LANGMUIR

Formation and Dynamics of Imidazole Supramolecular Chains Investigated by Deep Potential Molecular Dynamics Simulation

Published as part of Langmuir special issue "Highlighting Contributions from our Editorial Board Members in 2024".

Jianwei Zhang, Jinyu Lei, Pu Feng, Wenduo Chen, Jiajia Zhou,* and Guangzhao Zhang*

Cite This: *Langmuir* 2024, 40, 23864−23871

Read Online

ACCESS | Metrics & More | Article Recommendations | Supporting Information

ABSTRACT: Imidazole-based materials have attracted considerable attention due to their promising potential for facilitating anhydrous proton transport at high temperatures. Herein, a machine learning-based deep potential (DP) model for bulk imidazole with first-principles accuracy is developed. The trained model exhibits remarkable accuracy in predicting energies and forces, with minor errors of 4.71×10^{-4} eV/atom and 3.23×10^{-2} eV/Å, respectively. Utilizing DP molecular dynamics simulations, we have systematically investigated the temperature-dependent formation and dynamics of imidazole supramolecular chains through the partial radial distribution function, quantification of hydrogen bond numbers, incoherent intermediate scattering function, and diffusion coefficient. The findings reveal the influence of temperature on the proton transport path following either the "Grotthuss" and "vehicle" mechanism.

Formation and Dynamics of Imidazole Supramolecule
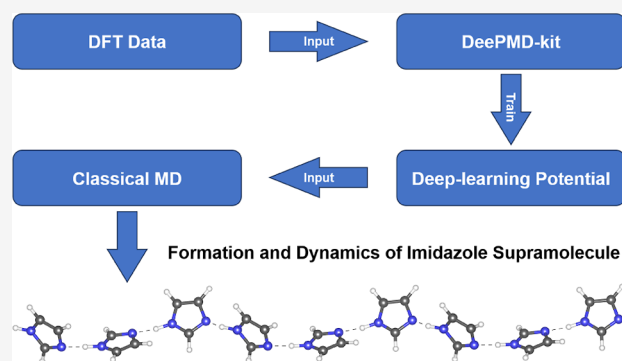
1. INTRODUCTION

Proton transport is essential for regulating enzymatic catalysis and bioenergetics in biological systems,[1,2] as well as for driving advancements in energy conversion and storage technologies like proton exchange membrane fuel cells.[3,4] The leading proton exchange membranes in use, Nafion membranes, rely heavily on the maintenance of embedded water channels for stable performance, necessitating high humidity and moderate temperatures (<80 °C).[5] However, a growing number of applications desire outstanding proton conductivity at higher temperatures (up to 200 °C), where retaining water molecules proves challenging.[6] For this purpose, imidazole and its derivatives have garnered significant interest for their non-volatile nature, high boiling points, and the capability to exist in two tautomeric forms that support a proton-transport pathway between the nitrogen atoms.[7−10] Proton transport in proton-conducting materials based on imidazole can occur via either the "vehicle" or "Grotthuss" mechanism.[11,12] The "vehicle" mechanism is contingent upon the diffusion of imidazole, and the "Grotthuss" mechanism relies on the reorientation of imidazole dipoles within the supramolecular chain linked by hydrogen bonds (HBs).[13] Previous studies have proved that confining imidazole within one-dimensional nanochannels significantly improves anhydrous proton conductivity, with the predominance of the "Grotthuss" mechanism.[13−15] Therefore, understanding the formation and

dynamics of the imidazole supramolecular chain and its temperature dependence is crucial for the design of proton exchange membranes with enhanced anhydrous proton conductivity.

As a powerful tool to investigate the dynamic properties in microscopic studies, atomistic simulations offer valuable information and insights that enhance and clarify the experimental findings. However, the high computational costs limit the application of ab initio molecular dynamics (AIMD) simulations to systems with a large number of atoms over extended time scales, thus posing a challenge when studying supramolecular systems. Though classical MD (CMD) simulation overcomes the scale problem, its accuracy is seriously affected by the empirical potential. Recently, novel machine learning potential models have emerged to confront the persistent challenge to combine both high accuracy and efficiency, including the Behler−Parrinello neural network,[16] the deep tensor neural network,[17] the bonds-in-molecules neural network,[18] the Gaussian approximation potentials,[19] the
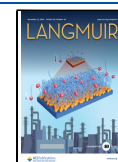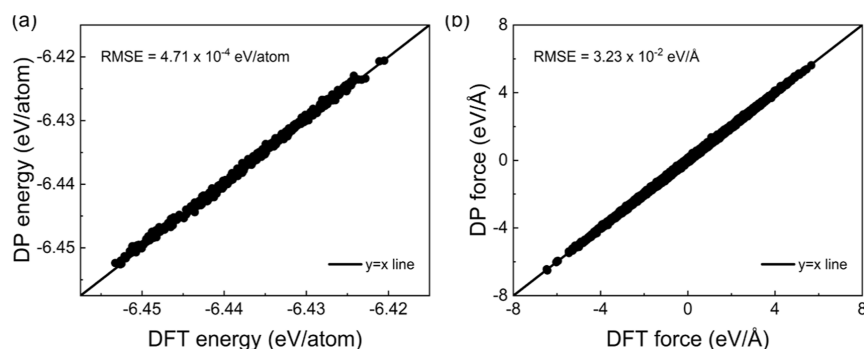
Figure 1. Comparison results between DFT calculation and DP prediction of (a) energy and (b) force for bulk imidazole at all temperatures.

gradient domain machine learning,[20] and the deep potential (DP).[21,22] For a diverse range of systems, MD simulations based on DP have exhibited efficiency competitive with CMD while achieving accuracy levels comparable to AIMD based on density functional theory (DFT).[23−27] In particular, DP has also been successfully applied to study systems with HB,[28,29] indicating its potential in investigating the dynamics of imidazole supramolecule systems.

In this work, we develop a DP for imidazole trained on DFT calculations and employ DPMD on a bulk system containing large quantities of imidazole at different temperatures. The DPMD results quantitatively demonstrate the temperature dependence of the formation and dynamics of imidazole supramolecular chains, which reflects the variation of the proton conduction path in the "Grotthuss" mechanism. The diffusion of imidazole has also been studied to reflect the proton transport in the "vehicle" mechanism. These findings are valuable in guiding the design of novel anhydrous proton-conducting materials that are effective across a wide range of temperatures.

2. METHODS

2.1. Data Generation and DP Training. In order to extensively generate training datasets for the DP model, we adopt the DP generator (DP-GEN) workflow.[30,31] The DP-GEN process involves three key steps in each iteration: training, exploration, and labeling. Through the implementation of a streamlined and efficient sampling technique, the requirement for extensive training data is reduced. This ensures the precision and dependability of the resulting surface potential energy surface model.

2.1.1. Initialization. AIMD simulations of bulk imidazole (16 imidazole molecules) at different temperatures (T = 313.15, 353.15, 393.15, 433.15, and 473.15 K) were performed by using the Vienna Ab initio Simulation Package (VASP) to initialize the DP-GEN workflow.[32,33] All of the first-principles calculations were performed based on DFT with all-electron projected augmented wave method.[34] Generalized gradient approximation with the Perdew−Burke−Ernzerhof (PBE) exchange correlation functional was employed.[35,36] The valence wave functions were expanded in a plane-wave basis with a cutoff energy of 500 eV. We used the Methfessel−Paxton method to determine partial occupancies with a smearing width of 0.05 eV. The k-point mesh and time step were set to $1 \times 1 \times 1$ and 1 fs for all calculations. The convergence criterion for an electronic self-consistent loop was set to 1.0×10^{-6} eV. Previous studies[37] have shown that dispersion-corrected DFT contributes significantly to computational accuracy, particularly in systems like water, which contains a high number of HB. Thus, the PBE functional with a D3 dispersion correction[38] was used. The simulation cell is initially equilibrated at the target temperature for 12 ps with the *NPT* ensemble to obtain the density for each system. Then, 6 ps NVT runs were performed at given temperatures, and configurations in the last 3

ps runs of each system (15,000 configurations in total) were extracted as the initial dataset for DP training. In addition, 1000 configurations of each system (5000 configurations in total) from another 6 ps *NVT* runs were extracted as the validation dataset to test the final DP model.

2.1.2. Training. Four distinct DP potential models were developed during the training step using the initial dataset. These models shared consistent fitted parameters, differing only in the random seed variations. Each model underwent 800,000 gradient descent steps using the Adam stochastic gradient descent method within the DeePMD-kit[39] package. The se_e2_a descriptor was utilized with a cutoff radius of 6 Å and a smoothing cutoff of 0.5 Å. The embedding and fitting nets consisted of three layers with nodes [50, 100, and 200] and [320, 320, and 320], respectively. The initial values for tunable prefactors in the loss function were set to $p_e^{start} = 2$, $p_e^{limit} = 10$ for energy error and $p_f^{start} = 1000$, $p_f^{limit} = 1$ for force error, respectively. No virial data is available in the dataset, so the virial prefactors are set to $p_v^{start} = p_v^{limit} = 0$.

2.1.3. Exploration. During the exploration stage, the DP-GEN employs the large-scale atomic/molecular massively parallel simulator (LAMMPS)[40] for DPMD simulation. This enables the exploration of the configuration space across different thermodynamic conditions. The exploration conditions set for each iteration in this work are listed in Table S1. In order to sample reasonable configures from DPMD trajectories, the model deviation σ was introduced, representing the maximum standard deviation of the predictions for the atomic forces

$$\sigma = \max_i \sqrt{\left\langle \|F_i - \langle F_i \rangle\|^2 \right\rangle} \tag{1}$$

where F_i describes the force acting on atom i predicted by the DP model and $\langle F_i \rangle$ denotes the average of four different DP models. The lower and upper trust levels for force errors $\sigma_{lo} = 0.07$ eV and $\sigma_{hi} = 0.25$ eV were used, based on the accuracy attainable with the trained DP model. Configurations exhibiting small deviations, $\sigma < \sigma_{lo}$, indicate that the current model can accurately describe them. Conversely, excessive force deviation, $\sigma > \sigma_{hi}$, signals that the trajectories may be nonphysical, which were consequently not collected. Only those configurations falling within the range $\sigma_{lo} < \sigma < \sigma_{hi}$ will be considered for DFT calculations in the labeling stage.

2.1.4. Labeling. During the labeling stage, candidate configurations from the exploration stage underwent single point energy calculations using DFT theory to gather the energy and force data. These labeled configurations were then incorporated into the training dataset for the subsequent training process. The exploration process was deemed converged when the percentage of the remaining candidate configurations reached exceedingly low levels.

Finally, the DP-GEN process completed 10 iterations and introduced 13,599 new configurations to the training dataset, bringing the total to 28,599 configurations. The accuracy improvement of the model in each iteration of the DP-GEN process is shown in Figure S1. The hyperparameters used in the final DP model are identical to those used during the training step in dataset generation, with the exception of the gradient descent training steps. A total of 1,200,000 steps were
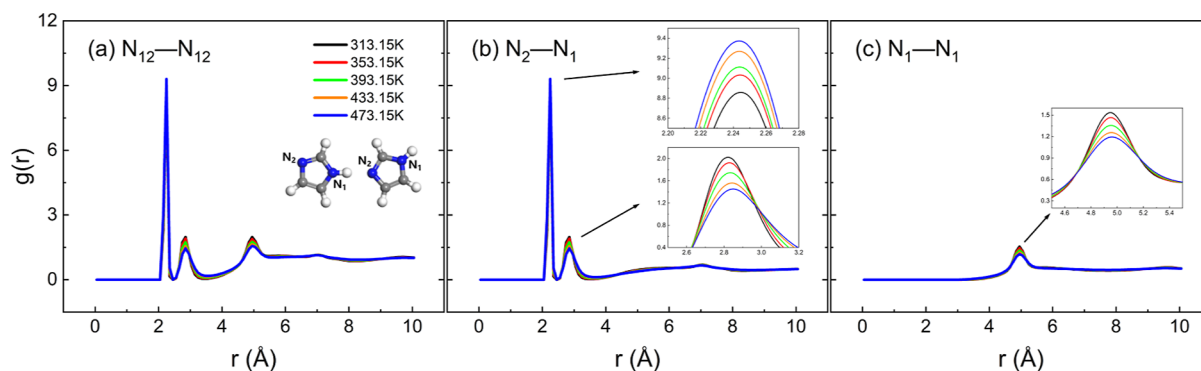
Figure 2. RDF $g(r)$ between (a) N_{12} and N_{12} atoms, (b) N_2 and N_1 atoms, and (c) N_1 and N_1 atoms.
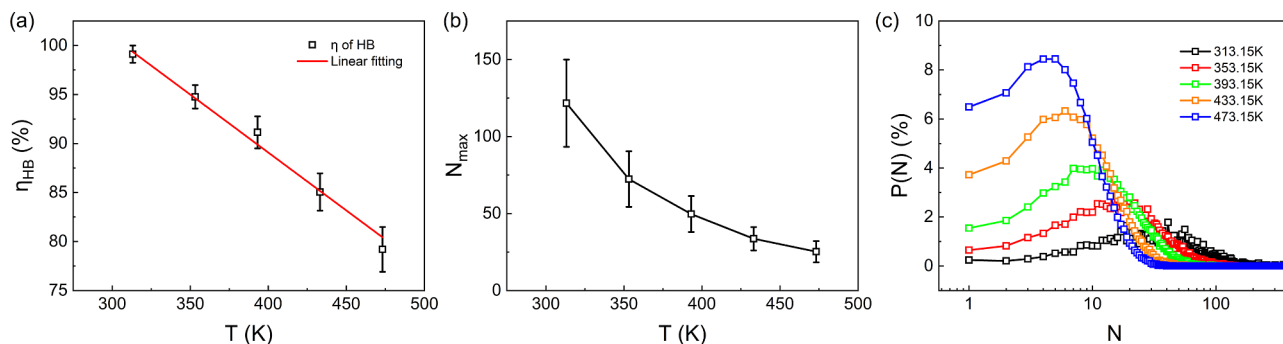

Figure 3. Temperature dependence of imidazole supramolecular chains formation, for (a) the efficiency of hydrogen bond formation η_{HB}, (b) the maximum degree of polymerization N_{max} of the chains, and (c) the probability distribution $P(N)$ of an imidazole supramolecular chain with a degree of polymerization N.

carried out to improve training accuracy and produce a high-fidelity DP model.

2.2. DPMD Simulations. DPMD simulations were performed based on the trained DP models using LAMMPS. In this stage, the number of imidazole molecules in the cell was increased to 1024, and the trajectories for analyzing the formation and dynamics of the imidazole supramolecular chain were generated. First, DPMD simulations were conducted in the NPT ensemble for 500 ps to determine the density. The result is well consistent with that of AIMD, as shown in Figure S2, which illustrates the trained DP model demonstrates comparable accuracy to AIMD. However, the densities obtained from both DPMD and AIMD simulations are lower than those from CMD simulations using the AMBER 94 force field.[41] This discrepancy can largely be attributed to the differences in accuracy between DFT calculations and CMD performed with a classical force field. Subsequently, simulations were run in the NVT ensemble for 1000 ps, and these trajectories were extracted for further analysis.

3. RESULTS AND DISCUSSION

3.1. Validation of DP Model. The validation of the DP model used in DPMD simulations was conducted by assessing the predicted atomic forces and total energy of bulk imidazole for the unseen configurations. The comparison results between the DFT calculation and the DP model predictions for all systems in energy and force (in the three spatial directions x, y, and z) are presented in Figure 1. Excellent diagonal distribution of both energy and force illustrates that the final DP model has a high precision to accurately reproduce the DFT results. The average root-mean-square errors (RMSE) of all systems equals to 4.71×10^{-4} eV/atom for energy prediction and 3.23×10^{-2} eV/Å for force prediction, respectively, which are sufficiently small.

For further validation of the final DP model, additional 6 ps AIMD simulations were conducted with the same density as that in DPMD simulations. The partial radial distribution function (RDF) of each system in both DPMD simulations and AIMD simulations was calculated by

$$g(r) = \frac{1}{4\pi\rho_\beta r^2}\frac{dN_{\alpha\beta}(r)}{dr} \tag{2}$$

where ρ_β denotes the number density of the β atom and $N_{\alpha\beta}(r)$ represents the average number of β atoms that lie in a sphere of radius r centered on an α atom. The RDF of nitrogen atoms at all temperatures in DPMD simulations is in good agreement with the AIMD results, as shown in Figure S3. The results suggest that the developed DP model is robust and capable of reproducing the first-principles calculation results.

3.2. Properties of Bulk Imidazole. In order to investigate the temperature effect on the formation of imidazole supramolecular chains, we mark the nitrogen atom with hydrogen within an imidazole molecule as a N_1 atom, and another as a N_2 atom. In addition, N_{12} atoms refer to when both N_1 and N_2 atoms are considered. The RDF between different types of nitrogen atoms for each system is depicted in Figure 2. The RDF between N_{12}—N_{12} atoms exhibits three prominent peaks located at approximately 2.25, 2.85, and 4.95 Å, as shown in Figure 2a. According to the structure of imidazole, the first peak predominantly arises from another nitrogen atom within the same imidazole molecule. The second peak is entirely attributed to the N_1 or N_2 atom of a different imidazole molecules involved in hydrogen bonding, since this peak is explicitly observed in the RDF between N_2—N_1 atoms and is completely absent at the same position in the
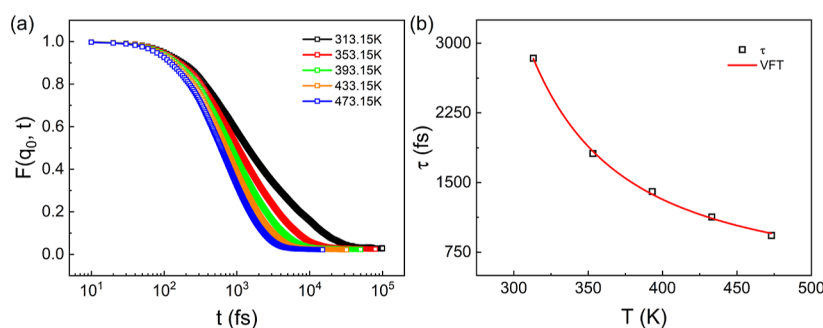
Figure 4. (a) Incoherent ISF $F(q_0, t)$ of the nitrogen atoms in bulk imidazole at all temperatures. (b) Characteristic segmental α-relaxation time τ_α as a function of temperature T.

RDF between N_1-N_1 atoms, as illustrated in Figure 2b,c. The third peak is mainly contributed by a nitrogen atom of the same type within the paired imidazole molecule, as shown in Figure 2c. With the rise in temperature, the density of the system decreases, leading to the higher first peak. By contrast, the height of the second peak decreases with the increasing temperature. This phenomenon signifies the broken of HB due to the elevated energy. Moreover, the higher the temperature, fewer the retained HB. The result illustrates that increasing temperature hinders the establishment of proton transport paths based on the "Grotthuss" mechanism.

Quantitative calculations were employed to investigate the temperature dependence of imidazole supramolecular chain formations. The number of HB in each system was determined based on the criterion that the N_1-N_2 atom distance is less than 3.5 Å and the N_1-H-N_2 angle is greater than 135°. The efficiency of HB formation η_{HB}, which also reflects the efficiency of constructing the proton transport path, is defined as the ratio of the number of formed HB and the maximum number of HB of the system. Since each HB involves two imidazole molecules, the maximum number of HB molecules should be equal to the total number of imidazole molecules. Therefore, the efficiency of HB formation can be expressed as

$$\eta_{HB} = \frac{n_{HB}}{n_{imi}} \times 100\% \tag{3}$$

where n_{HB} represents the average number of HB at certain temperature and n_{imi} denotes the total number of imidazole molecules. The data of n_{HB} were collected from the last 400 ps of DPMD simulations, as depicted in Figure S4a, and the data of η_{HB} are shown in Figure 3a. Within the temperature range from 313.15 to 473.15 K, η_{HB} has a good linear relation with temperature T, given by η_{HB} (%) $\approx -0.1182 \times T$ (K) $+ 136.4$.

The result shows higher efficiency of HB formation in bulk imidazole compared with previous study by CMD simulations using the AMBER 94 force field, as shown in Figure S5.[41] We deem it can be attributed to classical force fields having a relatively simple form, which struggles with accurately describing the HB. This result also demonstrates that DPMD is a promising method for a complex system. In addition, the observation in this work indicates that hydrogen atoms in all imidazole molecules will engage in HB formation at temperatures below approximately 308 K. Furthermore, we collected the degree of polymerization N for each imidazole supramolecular chain to demonstrate the length of the proton transport paths. The method for calculating the degree of polymerization N of the supramolecular chain involves using an imidazole molecule that forms only one HB as the chain

end unit. Imidazole molecules connected by HB are sequentially counted until another imidazole molecule, also forming a single HB, is encountered at the opposite chain end. The variation of the maximum degree of polymerization N_{max} of the chains with temperature was determined based on the data provided in Figure S4b, as shown in Figure 3b. The average value of N_{max} of the chains at 313.15 K can reach around 122, indicating a high level akin to that seen in conventional polymer systems. With the increase in temperature, the supramolecular chains gradually disassemble, and N_{max} decreases to around 25 at 473.15 K. To capture the polydispersity of the chains, the probability distribution $P(N)$ of an imidazole supramolecular chain with a degree of polymerization N was calculated at all temperatures by

$$P(N) = \frac{n_N \times N}{n_{imi}} \times 100\% \tag{4}$$

where n_N stands for the number of chains with a degree of polymerization N. As shown in Figure 3c, the distribution peak is extremely broad at 313.15 K and gradually narrows with increasing temperature. This trend indicates that while increasing the temperature leads to a reduction in the length of the proton transport path, it results in a more uniform distribution of path lengths. Furthermore, the maximum $P(N)$ values are observed at approximately $N = 28, 15, 9, 6$, and 4 when $T = 313.15, 353.15, 393.15, 433.15$, and 473.15 K, respectively. Previous studies indicate that the melting temperature of imidazole is approximately 363 K.[42] Therefore, in our simulation, 313.15 K is below the melting temperature, 353.15 K is near it, while 393.15, 433.15, and 473.15 K are above the melting temperature. At 353.15 K, the critical state of the solid−liquid transition, the system still maintains a high HB formation efficiency of approximately 94.8%. However, the average polymerization degree of chains falls below 15 and results in a molecular weight under 1000 g/mol, which shows the characteristics of oligomers.

For the "Grotthuss" mechanism, the reorientation of imidazole dipoles is directly related to the segmental α-relaxation within the supramolecular chain. Therefore, the incoherent intermediate scattering function (ISF) of the nitrogen atoms was calculated for each system using the expression

$$F(q_0, t) = \frac{1}{N_t} \left\langle \sum_{i=1}^{N_t} e^{-iq_0 \cdot [r_i(t) - r_i(0)]} \right\rangle \tag{5}$$

where N_t stands for the total number of the nitrogen atoms, $r_i(t)$ denotes the position of the ith atom at time t, and $q_0 \approx$
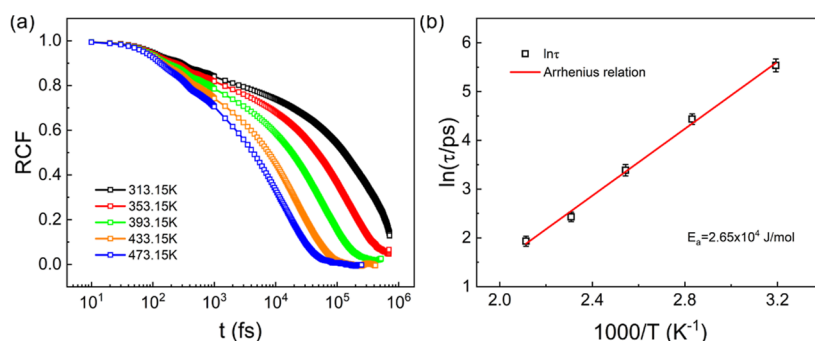
Figure 5. (a) Rotational correlation function RCF(t) of bulk imidazole molecules at all temperatures. (b) Characteristic time τ of rotation of imidazole dipoles as a function of temperature T.
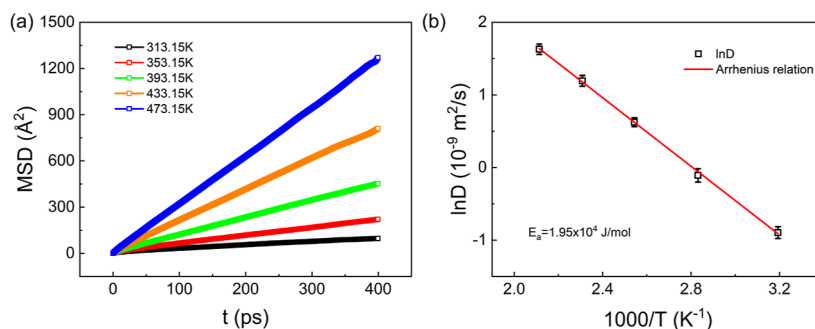

Figure 6. (a) MSD of imidazole as a function of time t at all temperatures. (b) Diffusion coefficient D of imidazole as a function of temperature T.

1.23 Å^{-1} corresponds to the position of the first peak in the static structure factor (SSF), as shown in Figure S6. Since the temperatures are relatively high, only one mode is observed in the decay of ISF, as indicated in Figure 4a. Additionally, the decay of ISF of bulk imidazole becomes significantly faster with the increase of temperature. The characteristic segmental α-relaxation time τ_α at each temperature is obtained according to the criterion $F(q_0, t) = e^{-(t/\tau_\alpha)^\beta}$, as depicted in Figure 4b. All relaxation times lie within the picosecond range throughout the temperature range studied and are well described by the Vogel–Fulcher–Tammann (VFT) relation[43]

$$\tau_\alpha(T) = \tau_0 \exp\left(\frac{BT_0}{T - T_0}\right) \tag{6}$$

where B is a basic parameter describing the strength of the temperature dependence of relaxation in glass-forming liquids, and T_0 is referred to as the Vogel temperature that can be considered as the glass-transition temperature (T_g) in ideal glasses.[44] The fitting result shows $B \approx 2.38$ and $T_0 \approx 150$ K, demonstrating the onset temperature of the "Grotthuss" mechanism. Furthermore, to establish a correlation with neutron scattering experiments, we calculated both the SSF and ISF of hydrogen atoms bonded to nitrogen, as shown in Figures S7 and S8a. The segmental relaxation dynamics are also effectively represented by these hydrogen atoms, with VFT fitting results showing $B \approx 2.26$ and $T_0 \approx 167$ K, as shown in Figure S8b.

Another important quantity that can reflect the reorientation of imidazole dipoles is the rotational correlation function (RCF).[45] We calculated the RCF of bulk imidazole molecules following expression

$$\text{RCF}(t) = \langle \mathbf{e}_i(t + t_0) \bullet \mathbf{e}_i(t_0) \rangle \tag{7}$$

where angular brackets denote ensemble averages and $\mathbf{e}_i$ is a unit vector rotating with molecule i. Herein, we used the unit vector of the N_1 atom to N_2 atom as $\mathbf{e}_i$ of an imidazole molecule. The results are plotted in Figure 5a. From the criterion $\text{RCF}(t) = e^{-(t/\tau)^\beta}$, the characteristic time τ of rotation of imidazole dipoles was obtained, as shown in Figure 5b. The relation between characteristic time τ and temperature T is described by the Arrhenius relation

$$\tau(T) = A \exp\left(\frac{E_a}{RT}\right) \tag{8}$$

where E_a represents the activation energy and A is the constant prefactor. The fitting result shows that $A \approx 4.67$ fs, and the activation energy for rotation of imidazole dipoles is $E_a \approx 2.65 \times 10^4$ J/mol. Note that in this work, we primarily focus on the formation and dynamics of imidazole supramolecular chains, without providing excess protons for conduction. The absence of transient chain breakage during proton conduction results in greater stability of the imidazole molecules within the supramolecular chain. Consequently, the rotation of a single imidazole molecule within the stable supramolecular chain is challenging. The activation energy obtained in this case may be higher than that during proton conduction.

To evaluate the proton transport capacity of imidazole through the "vehicle" mechanism, the mean square displacement (MSD) of imidazole was calculated as a function of time t for different temperatures by

$$\text{MSD}(t) = \langle [x_i(t) - x_i(0)]^2 + [y_i(t) - y_i(0)]^2 \\ + [z_i(t) - z_i(0)]^2 \rangle \tag{9}$$

where x_i, y_i, and z_i represent the coordinates of the ith nitrogen atom in bulk imidazole. The linear MSD curves depicted in

Figure 6a indicate that the diffusion mechanism of imidazole within supramolecular chains is still dominated by Brownian motion. Subsequently, the diffusion coefficient of imidazole was obtained according to the MSD using the Einstein equation

$$D = \lim_{t \to \infty} \frac{\text{MSD}(t)}{2dt} \tag{10}$$

where d stands for the dimensionality of the system, which is equal to 3 in this work. As shown in Figure 6b, increasing the temperature can improve the diffusion coefficient of imidazole so that it enhances the proton transport over the desired temperature range; however, the improvement is no more than an order of magnitude. Moreover, the relation between diffusion coefficient D and temperature T is well described by the Arrhenius relation

$$D(T) = D_0 \exp\left(\frac{-E_a}{RT}\right) \tag{11}$$

where E_a represents the activation energy for diffusion and D_0 represents pre-exponential factor, which can be considered as the diffusion coefficient at extremely high temperatures. The fitting result shows that $D_0 \approx 7.31 \times 10^{-7}$ m^2/s and the diffusion of imidazole molecules is activated by $E_a \approx 1.95 \times 10^4$ J/mol. Previous study[41] demonstrates that the activation energy obtained from HB lifetimes for the bulk imidazole, which represents the energy required to break HB, is 8.7×10^3 J/mol, lower than the activation energy for the diffusion of imidazole molecules. This illustrates that as the temperature increases the HB within solid imidazole begin to break, allowing for HB exchange and reorientation of imidazole dipoles. At this stage, proton conduction primarily relies on the "Grotthuss" mechanism. With further temperature elevation, both the efficiency of HB formation and the polymerization degree of supramolecules decrease, leading to a reduction in proton conduction pathways based on the "Grotthuss" mechanism. Simultaneously, imidazole undergoes melting, enhancing the self-diffusion capability of molecules in the bulk. The proton conduction gradually balances between the "Grotthuss" mechanism and the "vehicle" mechanism.

4. CONCLUSIONS

In conclusion, we developed a high-accuracy DP model for bulk imidazole and systematically investigated the temperature-dependent formation and dynamics of imidazole supramolecular chains by DPMD simulations. The DP model was established through an iterative training approach involving compressed and expanded starting structures coupled with DFT calculations and active learning. The performance of the DP model was assessed by calculating the RMSE for energy and force as well as comparing the RDF of bulk imidazole in both AIMD and DPMD simulations. The maximum RMSE values obtained were 4.71×10^{-4} eV/atom for energy and 3.23×10^{-2} eV/Å for force, indicating strong predictive capability. In addition, the RDF of nitrogen atoms in imidazole from DPMD simulations closely matched the AIMD outcomes across all temperatures. These results indicate that the well-trained DP model is capable of accurately describing the system of bulk imidazole.

Utilizing the DP model, we successfully simulated a large cell comprising 1024 imidazole molecules with first-principles accuracy and generated a trajectory length of 1 ns for in-depth analysis. The DPMD results revealed a decrease in the number of HB in bulk imidazole with an increase in temperature, as evidenced by the declining height of the second peak in the RDF of nitrogen atoms. From 313.15 to 473.15 K, a good linear relation between the efficiency of HB formation and temperature was obtained as η_{HB} (%) $\approx -0.1182 \times T$ (K) + 136.4, and N_{max} of imidazole supramolecular chains decreases intensively from approximately 122 to 25. The distribution of N of the chains is extremely broad at 313.15 K and gradually narrows with increasing temperature. Furthermore, the maximum probability of N of the formed supramolecular chains appears at approximately $N = 28$, 15, 9, 6, and 4 when the temperature is 313.15, 353.15, 393.15, 433.15, and 473.15 K, respectively. Regarding the dynamics of imidazole supramolecular chains, the characteristic segmental α-relaxation time τ_α was observed within the picosecond range across the temperature range of 313.15 to 473.15 K. The glass-transition temperature of the supramolecular chain was identified as 150 K according to the VFT relation. Moreover, within the temperature range of 313.15 to 473.15 K, the diffusion coefficient of imidazole is approximately 10^{-9} m^2/s, showing a variation of not more than 1 order of magnitude. The activation energy of diffusion was determined as $E_a \approx 1.95 \times 10^4$ J/mol. The insights presented in this study may contribute to a deeper understanding of the effective proton transport through both the "Grotthuss" and "vehicle" mechanisms in imidazole-based materials.

■ ASSOCIATED CONTENT

Ⓢ Supporting Information

The Supporting Information is available free of charge at https://pubs.acs.org/doi/10.1021/acs.langmuir.4c02888.

Parameters in the DP-GEN workflow, density of bulk imidazole, RDF, and formation of HB, SSF, and ISF (PDF)

■ AUTHOR INFORMATION

Corresponding Authors

Jiajia Zhou − *South China Advanced Institute for Soft Matter Science and Technology, School of Emergent Soft Matter and Guangdong Provincial Key Laboratory of Functional and Intelligent Hybrid Materials and Devices, South China University of Technology, Guangzhou 510640, China;* Ⓞ orcid.org/0000-0002-2258-6757; Email: zhouj2@scut.edu.cn

Guangzhao Zhang − *Faculty of Materials Science and Engineering, South China University of Technology, Guangzhou 510640, China;* Ⓞ orcid.org/0000-0002-0219-3729; Email: msgzzhang@scut.edu.cn

Authors

Jianwei Zhang − *Faculty of Materials Science and Engineering, South China University of Technology, Guangzhou 510640, China*

Jinyu Lei − *Faculty of Materials Science and Engineering, South China University of Technology, Guangzhou 510640, China*

Pu Feng − *School of Civil Engineering and Transportation, South China University of Technology, Guangzhou 510640, China*

Wenduo Chen − *School of Materials, Sun Yat-sen University, Guangzhou 510275, China*

■ **REFERENCES**

(1) Kreuer, K. D. Proton conductivity: materials and applications. *Chem. Mater.* **1996**, *8*, 610−641.

(2) Lee, J.; Choe, I. R.; Kim, Y. O.; Namgung, S. D.; Jin, K.; Ahn, H. Y.; Sung, T.; Kwon, J. Y.; Lee, Y. S.; Nam, K. T. Proton conduction in a tyrosine-rich peptide/manganese oxide hybrid nanofilm. *Adv. Funct. Mater.* **2017**, *27*, 1702185.

(3) Xiao, F.; Wang, Y. C.; Wu, Z. P.; Chen, G.; Yang, F.; Zhu, S.; Siddharth, K.; Kong, Z.; Lu, A.; Li, J. C.; et al. Recent advances in electrocatalysts for proton exchange membrane fuel cells and alkaline membrane fuel cells. *Adv. Mater.* **2021**, *33*, 2006292.

(4) Li, H.; Zhao, H.; Jian, S.; Tao, B.; Gu, S.; Xu, G.; Wang, G.; Chang, H. Designing proton exchange membrane fuel cells with high specific power density. *J. Mater. Chem. A* **2023**, *11*, 17373−17391.

(5) Prykhodko, Y.; Fatyeyeva, K.; Hespel, L.; Marais, S. Progress in hybrid composite Nafion®-based membranes for proton exchange fuel cell application. *Chem. Eng. J.* **2021**, *409*, 127329.

(6) Haider, R.; Wen, Y.; Ma, Z.; Wilkinson, D. P.; Zhang, L.; Yuan, X.; Song, S.; Zhang, J. High temperature proton exchange membrane fuel cells: progress in advanced materials and key technologies. *Chem. Soc. Rev.* **2021**, *50*, 1138−1187.

(7) Scheiner, S.; Yi, M. Proton transfer properties of imidazole. *J. Phys. Chem.* **1996**, *100*, 9235−9241.

(8) Münch, W.; Kreuer, K. D.; Silvestri, W.; Maier, J.; Seifert, G. The diffusion mechanism of an excess proton in imidazole molecule chains: first results of an ab initio molecular dynamics study. *Solid State Ionics* **2001**, *145*, 437−443.

(9) Daycock, J. T.; Jones, G. P.; Evans, J. R. N.; Thomas, J. M. Rotation of imidazole in the solid state and its significance in deciding the nature of charge migration in biological materials. *Nature* **1968**, *218*, 672−673.

(10) Dey, B.; Debnath, P.; Chakraborty, S.; Deb, B.; Bhattacharjee, D.; Majumdar, S.; Hussain, S. A. Study of compression-induced supramolecular nanostructures of an imidazole derivative by Langmuir−Blodgett technique. *Langmuir* **2017**, *33*, 8383−8394.

(11) Kreuer, K. D.; Rabenau, A.; Weppner, W. Vehicle mechanism, a new model for the interpretation of the conductivity of fast proton conductors. *Angew. Chem., Int. Ed. Engl.* **1982**, *21*, 208−209.

(12) Agmon, N. The Grotthuss mechanism. *Chem. Phys. Lett.* **1995**, *244*, 456−462.

(13) Cai, L.; Yang, J.; Lai, Y.; Liang, Y.; Zhang, R.; Gu, C.; Kitagawa, S.; Yin, P. Dynamics and proton conduction of heterogeneously confined imidazole in porous coordination polymers. *Angew. Chem., Int. Ed. Engl.* **2023**, *62*, No. e202211741.

(14) Bureekaew, S.; Horike, S.; Higuchi, M.; Mizuno, M.; Kawamura, T.; Tanaka, D.; Yanai, N.; Kitagawa, S. One-dimensional imidazole aggregate in aluminium porous coordination polymers with high proton conductivity. *Nat. Mater.* **2009**, *8*, 831−836.

(15) Ye, Y.; Zhang, L.; Peng, Q.; Wang, G.-E.; Shen, Y.; Li, Z.; Wang, L.; Ma, X.; Chen, Q.-H.; Zhang, Z.; Xiang, S. High anhydrous proton conductivity of imidazole-loaded mesoporous polyimides over a wide range from subzero to moderate temperature. *J. Am. Chem. Soc.* **2015**, *137*, 913−918.

(16) Behler, J.; Parrinello, M. Generalized neural-network representation of high-dimensional potential-energy surfaces. *Phys. Rev. Lett.* **2007**, *98*, 146401.

(17) Schütt, K. T.; Arbabzadah, F.; Chmiela, S.; Müller, K. R.; Tkatchenko, A. Quantum-chemical insights from deep tensor neural networks. *Nat. Commun.* **2017**, *8*, 13890.

(18) Yao, K.; Herr, J. E.; Brown, S. N.; Parkhill, J. Intrinsic bond energies from a bonds-in-molecules neural network. *J. Phys. Chem. Lett.* **2017**, *8*, 2689−2694.

(19) Bartók, A. P.; Payne, M. C.; Kondor, R.; Csányi, G. Gaussian approximation potentials: the accuracy of quantum mechanics, without the electrons. *Phys. Rev. Lett.* **2010**, *104*, 136403.

(20) Chmiela, S.; Tkatchenko, A.; Sauceda, H. E.; Poltavsky, I.; Schütt, K. T.; Müller, K. R. Machine learning of accurate energy-conserving molecular force fields. *Sci. Adv.* **2017**, *3*, No. e1603015.

(21) Zhang, L.; Han, J.; Wang, H.; Car, R.; E, W. Deep potential molecular dynamics: a scalable model with the accuracy of quantum mechanics. *Phys. Rev. Lett.* **2018**, *120*, 143001.

(22) Han, J.; Zhang, L.; Car, R. Deep potential: a general representation of a many-body potential energy surface. *Commun. Comput. Phys.* **2018**, *23*, 629−639.

(23) Achar, S. K.; Wardzala, J. J.; Bernasconi, L.; Zhang, L.; Johnson, J. K. Combined deep learning and classical potential approach for modeling diffusion in UiO-66. *J. Chem. Theory Comput.* **2022**, *18*, 3593−3606.

(24) Zhang, L.; Wang, H.; Car, R.; E, W. Phase diagram of a deep potential water model. *Phys. Rev. Lett.* **2021**, *126*, 236001.

(25) Malosso, C.; Zhang, L.; Car, R.; Baroni, S.; Tisi, D. Viscosity in water from first-principles and deep-neural-network simulations. *npj Comput. Mater.* **2022**, *8*, 139.

(26) Zeng, J.; Tao, Y.; Giese, T. J.; York, D. M. QDπ: a quantum deep potential interaction model for drug discovery. *J. Chem. Theory Comput.* **2023**, *19*, 1261−1275.

(27) Zhao, J.; Feng, T.; Lu, G.; Yu, J. Insights into the local structure evolution and thermophysical properties of NaCl-KCl-MgCl2-LaCl3 melt driven by machine learning. *J. Mater. Chem. A* **2023**, *11*, 23999−24012.

(28) Ryu, J. H.; Yu, J. W.; Yoon, T. J.; Lee, W. B. Understanding the dielectric relaxation of liquid water using neural network potential and classical pairwise potential. *J. Mol. Liq.* **2024**, *397*, 124054.

(29) Liu, R.; Chen, M. Characterization of the hydrogen-bond network in high-pressure water by deep potential molecular dynamics. *J. Chem. Theory Comput.* **2023**, *19*, 5602−5608.

(30) Zhang, Y.; Wang, H.; Chen, W.; Zeng, J.; Zhang, L.; Wang, H.; E, W. DP-GEN: a concurrent learning platform for the generation of reliable deep learning based potential energy models. *Comput. Phys. Commun.* **2020**, *253*, 107206.

(31) Zhang, L.; Lin, D.-Y.; Wang, H.; Car, R.; E, W. Active learning of uniformly accurate interatomic potentials for materials simulation. *Phys. Rev. Mater.* **2019**, *3*, 023804.

(32) Kresse, G.; Furthmüller, J. Efficiency of ab-initio total energy calculations for metals and semiconductors using a plane-wave basis set. *Comput. Mater. Sci.* **1996**, *6*, 15−50.

(33) Kresse, G.; Furthmüller, J. Efficient iterative schemes for ab initio total-energy calculations using a plane-wave basis set. *Phys. Rev. B* **1996**, *54*, 11169−11186.

(34) Blöchl, P. E. Projector augmented-wave method. *Phys. Rev. B* **1994**, *50*, 17953−17979.

(35) Perdew, J. P.; Burke, K.; Ernzerhof, M. Generalized gradient approximation made simple. *Phys. Rev. Lett.* **1996**, *77*, 3865−3868.

(36) Zhang, Y.; Yang, W. Comment on "generalized gradient approximation made simple". *Phys. Rev. Lett.* **1998**, *80*, 890.

(37) Wohlfahrt, O.; Dellago, C.; Sega, M. Ab initio structure and thermodynamics of the RPBE-D3 water/vapor interface by neural-network molecular dynamics. *J. Chem. Phys.* **2020**, *153*, 144710.

(38) Grimme, S.; Antony, J.; Ehrlich, S.; Krieg, H. A consistent and accurate ab initio parametrization of density functional dispersion

correction (DFT-D) for the 94 elements H-Pu. *J. Chem. Phys.* **2010**, *132*, 154104.

(39) Wang, H.; Zhang, L.; Han, J.; E, W. DeePMD-kit: a deep learning package for many-body potential energy representation and molecular dynamics. *Comput. Phys. Commun.* **2018**, *228*, 178−184.

(40) Plimpton, S. Fast parallel algorithms for short-range molecular dynamics. *J. Comput. Phys.* **1995**, *117*, 1−19.

(41) Harvey, J. A.; Basak, D.; Venkataraman, D.; Auerbach, S. M. Simulating hydrogen-bond clustering and phase behaviour of imidazole oligomers. *Mol. Phys.* **2012**, *110*, 957−966.

(42) Kawada, A.; Mcghie, A. R.; Labes, M. M. Protonic conductivity in imidazole single crystal. *J. Chem. Phys.* **1970**, *52*, 3121−3125.

(43) Vargas-Lara, F.; Pazmiño Betancourt, B. A.; Douglas, J. F. Influence of knot complexity on glass-formation in low molecular mass ring polymer melts. *J. Chem. Phys.* **2019**, *150*, 101103.

(44) Gu, G. Y.; Bouvier, S.; Wu, C.; Laura, R.; Rzeznik, M.; Abraham, K. M. 2-Methoxyethyl (methyl) carbonate-based electrolytes for Li-ion batteries. *Electrochim. Acta* **2000**, *45*, 3127−3139.

(45) Gautam, S.; Le, T. T. B.; Rother, G.; Jalarvo, N.; Liu, T.; Mamontov, E.; Dai, S.; Qiao, Z.; Striolo, A.; Cole, D. Effects of water on the stochastic motions of propane confined in MCM-41-S pores. *Phys. Chem. Chem. Phys.* **2019**, *21*, 25035−25046.